# Global propagation of ionospheric disturbances associated with the 2022 Tonga Volcanic Eruption

David R Themens[1], Chris Watson[2], Nedjeljka Žagar[3], Sergiy Vasylkevych[3], Sean Elvidge[1], Anthony Mccaffrey[2], Paul Prikryl[2], Ben Reid[2], Alan Wood[1], and P T Jayachandran[2]

[1]University of Birmingham
[2]University of New Brunswick
[3]Universität Hamburg

November 22, 2022

## Abstract

In this study, we use measurements from over 4,735 globally distributed Global Navigation Satellite System (GNSS) receivers to track the progression of travelling ionospheric disturbances (TIDs) associated with the 15 January 2022 Hunga Tonga-Hunga Ha'apai submarine volcanic eruption. We identify two distinct Large Scale TIDs (LSTIDs) and several subsequent Medium Scale TIDs (MSTIDs) that propagate radially outward from the eruption site. Within 3000 km of epicenter, LSTIDs of >1600 km and ~1350 km wavelengths are initially observed propagating at speeds of ~950 ms-1 and ~555 ms-1, before substantial slowing to ~600 ms-1 and ~390 ms-1, respectively. MSTIDs with speeds of 200-400 ms-1 are observed for six hours following eruption, the first of which comprises the dominant global ionospheric response and coincides with the atmospheric surface pressure disturbance associated with the eruption. These are the first results demonstrating the global impact of the Tonga eruption on the ionospheric state.

# Global propagation of ionospheric disturbances associated with the 2022 Tonga Volcanic Eruption

David R. Themens[1,2], Chris Watson[2], Nedjeljka Žagar[3], Sergiy Vasylkevych[3], Sean Elvidge[1],

Anthony McCaffrey[2], Paul Prikryl[2], Ben Reid[2], Alan Wood[1], and P.T. Jayachandran[2]

1) Space Environment and Radio Engineering Group (SERENE), University of Birmingham, Birmingham, UK

2) Department of Physics, University of New Brunswick, Fredericton, NB, Canada

3) Meteorologisches Institut, Universität Hamburg, Hamburg, Germany

# Abstract

In this study, we use measurements from over 4,735 globally distributed Global Navigation Satellite System (GNSS) receivers to track the progression of travelling ionospheric disturbances (TIDs) associated with the 15 January 2022 Hunga Tonga-Hunga Ha'apai submarine volcanic eruption. We identify two distinct Large Scale TIDs (LSTIDs) and several subsequent Medium Scale TIDs (MSTIDs) that propagate radially outward from the eruption site. Within 3000 km of epicenter, LSTIDs of >1600 km and ~1350 km wavelengths are initially observed propagating at speeds of ~950 ms$^{-1}$ and ~555 ms$^{-1}$, before substantial slowing to ~600 ms$^{-1-}$ and ~390 ms$^{-1}$, respectively. MSTIDs with speeds of 200-400 ms$^{-1}$ are observed for six hours following eruption, the first of which comprises the dominant global ionospheric response and coincides with the atmospheric surface pressure disturbance associated with the eruption. These are the first results demonstrating the global impact of the Tonga eruption on the ionospheric state.

Key Points:

1) Highly directional LSTIDs are generated from the Tonga Eruption at initial speeds up to 950 m/s and propagate potentially as far as 20,000km.

2) Outside the local area of the eruption, MSTIDs coincident with the surface pressure wave form the dominant ionospheric response.

3) Secondary MSTIDs continue to be produced in the vicinity of the eruption for up to 6 hours following the event.

# Plain-Language Summary

The 2022 Tonga oceanic volcanic eruption and resulting tsunami was an incredibly impulsive and high energy event. Such events can generate strong pressure waves in the atmosphere that can propagate up into the Earth's ionosphere and modulate the plasma therein. Using every available Global Navigation Satellite System (GNSS) receiver from a global network of over 4,735 instruments, we were able to track the propagation of these waves from the Tonga eruption site around the planet. We show that an initial shock front at speeds up to 950 $ms^{-1}$ strongly perturb the ionospheric electron density near the eruption site and within a narrow extended region to the North, while smaller, slower waves originating from the eruption make up the strongest ionospheric response at distances far away from the eruption region. Small scale ionospheric waves continue to be produced near the eruption for up to six hours after the eruption began. These waves were tracked from the eruption to over 20,000km from the epicenter and could very well have persisted beyond the one day studied here.

## Introduction

Volcanic eruptions, earthquakes, atmospheric convective systems, and tsunamis have long been shown to invoke measurable ionospheric wave responses that can travel thousands of kilometers [Heki 2006; Dautermann et al., 2009; Tsugawa et al., 2011; Komjathy et al., 2012; Nishioka et al., 2013; Chou et al., 2017; Chen et al., 2017; Savastano et al., 2017; Inchin et al., 2020]. The acoustic and gravity waves (AGWs) and Rayleigh waves (RWs) resulting from these disturbances in the lower atmosphere and ocean [Mayr et al., 1984a; 1984b] can form traveling ionospheric disturbances (TIDs). These TIDs can cause minor perturbations in the integrated electron density of the ionosphere [Dautermann et al., 2009; Komjathy et al., 2016] and, in more severe cases, significant ionospheric tilting that has substantial implications for radio propagation at High Frequencies (HF) due to off-great circle propagation [Zawdie et al., 2016; Cervera and Harris, 2014]. With Global Navigation Satellite Systems (GNSS) we can track the progression of these waves in near real time [Savastano et al., 2017] and may soon provide operators with corrections necessary to ensure the resiliency of their systems to TID effects. In this study, we investigate the progression of TIDs as they circumnavigate the globe following the Hunga Tonga-Hunga Ha'apai (herein simply referred to as Tonga) underwater volcanic eruption and associated tsunami in January 2022.

Previous studies of the 2011 Tohoku earthquake and tsunami showed the generation of fast (3457 ms$^{-1}$) concentric Large Scale Traveling Ionospheric Disturbances (LSTIDs) associated with an RW that quickly dissipated at ranges of ~1000 km from the source, followed by Medium Scale TIDs with velocities in the range of 138-423 ms$^{-1}$ [Tsugawa et al., 2011]. Savastano et al. [2017] demonstrated the real time tracking of earthquake and tsunami-related ionospheric disturbances, finding wave propagation speeds of 316 ms$^{-1}$ for ionospheric structures induced by

82   the 2012 Haida Gwaii earthquake, consistent with the acoustic speed. More recently, Inchin et al.

83   [2020] and Zettergren and Snively [2019] used sophisticated atmospheric wave propagation

84   modeling to explore the causes and behavior of earthquake-induced TIDs and demonstrated

85   considerable non-linear effects and a high degree of anisotropy in the propagation of AGWs and

86   RWs associated with earthquakes.

87   Unfortunately, due to observational limitations most studies rarely examine the global

88   impact of such events. To examine whether the global coverage GNSS observational capacity

89   and the sheer impulsive size of this event would allow us to track these structures from

90   production to dissipation, we have here gathered data from every public GNSS receiver network

91   available to the authors and explore the behavior of ionospheric TIDs generated by the Tonga

92   volcanic eruption that began at 04:15 UT January 15 2022, centered at  (20.546$^{o}$S, 175.390$^{o}$W)

93   (https://earthquake.usgs.gov/earthquakes/eventpage/pt22015050/origin/detail).

94

## Data

96

97   GNSS measurements have long represented a vital dataset in the study of the global

98   ionospheric response to a wealth of phenomena. Using measurements of carrier phase and code

99   pseudorange on a pair of UHF signals, the integrated electron density of the ionosphere can be

100  found [Themens et al., 2013]. One can relate the integrated electron density along the GNSS ray

101  path, i.e. the Total Electron Content (TEC), to the phase difference on two signals via the

102  following

$$sTEC = \frac{1}{A}\left(\frac{f_1^2 f_2^2}{f_1^2 - f_2^2}\right)(\Delta L + W + rDCB + sDCB) \#(1)$$

103  where $A = 40.3$, $f_i$ is the first or second signal frequency, $\Delta L$ is the carrier phase difference

104  between the two signals, $W$ is a phase leveling parameter used to correct phase cycle ambiguities

105  with code measurements, $rDCB$ is the receiver Differential Code Bias (DCB), and $sDCB$ is the

106  satellite DCB. For this study, we make use of only Global Positioning System (GPS)

107  constellation measurements in the L1 C/A - L2P combination. To take advantage of the

108  exceptional precision of carrier phase measurements, one would generally "phase level" the

109  carrier TEC to that from the code pseudorange measurements using a satellite elevation

110  weighting, as in Themens et al. [2013]. In this study, we are interested solely in the relative

111  variations in TEC, which are typically calculated by applying a high-pass filter to un-leveled, un-

112  bias-corrected slant TEC (sTEC) [Komjathy et al., 2012; Zhang et al., 2019]. This approach,

113  however, can lead to an elevation dependence in the amplitude of variations due to the slant

114  propagation path. To mitigate this potential artifact, we instead opt to level our phase sTEC

115  measurements to pseudorange sTEC, apply satellite bias estimates from the Center for Orbit

116  Determination (CODE) (ftp://ftp.aiub.unibe.ch/), and then apply the Ma and Maruyama [2003]

117  receiver bias estimation method to get a first-order estimate of the absolute TEC. By removing

118  biases and phase-leveling, we can project the sTEC to vertical TEC (vTEC) using the standard

119  thin ionospheric shell model with a shell height of 400 km [Themens et al., 2015] without also

120  imposing a significant projection function-dependent trend to the vTEC [Themens et al., 2015].

121      This vTEC is then detrended by removing the 30-minute-wide, boxcar smoothed vTEC

122  from the unsmoothed vTEC, which is consistent with what has been used previously in studies of

123  the global propagation of MSTIDs and Large-Scale TIDs (LSTIDs) in Zhang et al. [2019];

124  however, as noted in Coster et al. [2017], the length of the chosen detrending window can have

125  an impact on the characteristics of the residual waves. Use a detrending window that is too wide

126  and you risk introducing substantial trends from quiescent ionospheric variability and masking

127  smaller scale structures behind stronger large-scale variability. Use a detrending window that is

128  too narrow and you risk removing parts of the desired signal. In our case, we sit on the boundary

129  of these two scenarios, where we have both LSTIDs and MSTIDs of interest. Using the 30-

130  minute window will allow us to easily identify the MSTIDs, but may artificially suppress the

131  observed amplitude of LSTID structures.

132      To further ensure the reliability of the data, any intervals with missing data, such as

133  partial intervals at the start of arcs of lock or across cycle slip events are omitted to ensure the

134  consistency of the smoothing interval and mitigate the impact of some cycle slips. Accounting

135  for DCBs may be an unnecessary step as the detrending process would remove slow moving

136  trends imposed by erroneous DCB projections, but we still apply DCB corrections as a

137  precautionary measure. To limit the amount of horizontal smearing by oblique ray paths, a lower
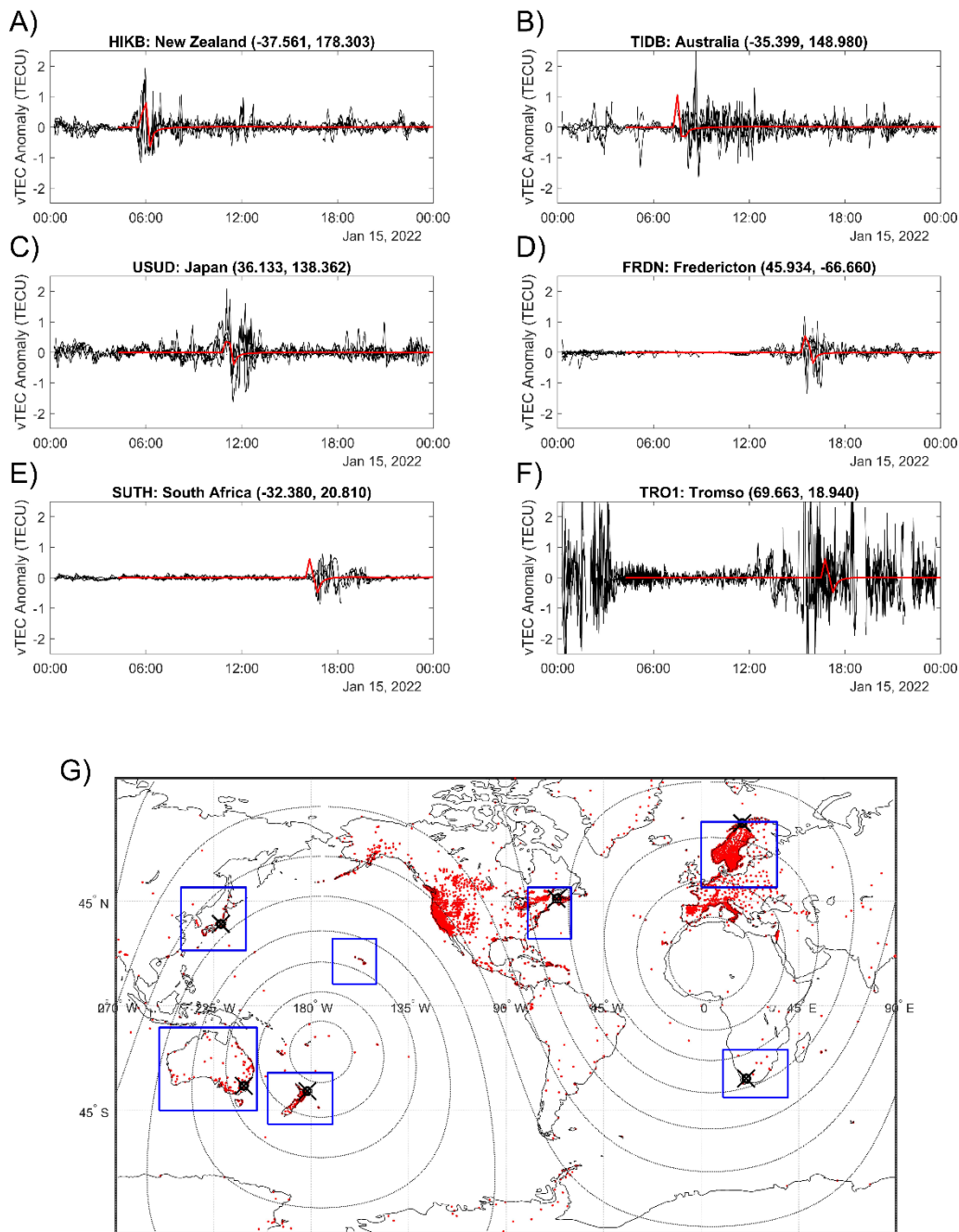
138  elevation limit of 40 degrees is used.

**Figure 1.** *Examples of vTEC anomalies (black) and shallow water layer thickness anomaly in units of 0.01 meters (red) for stations in New Zealand (A), Australia (B), Japan (C), Peru (D), Eastern Canada (E), and South Africa (F). Panel G: Map of GNSS receiver stations used in this study (red). The locations of the stations in (A)-(F) are marked with black 'x' symbols. Lines of constant distance from the eruption epicenter in 1,500km steps are presented as dotted lines. Blue boxes correspond to the domains used for the analysis in Figure 4.*

147       An example of the detrended vTEC at several stations in New Zealand (A), Australia (B),

148    Japan (C), Eastern Canada (D), South Africa (E), and Northern Europe (F) is presented in Figure

149    1. To track the propagation of these waves globally, we have gathered data from 4,735

150    distributed GNSS receivers from dozens of local and global receiver networks. These stations

151    correspond to all public data that were available within two days of the eruption. A map of the

152    stations used is presented in Figure 1G, with the sample stations from Figure 1A-F marked with

153    crosses.

154       The aforementioned processing is applied to each receiver, the ionospheric pierce points

155    (IPPs) of the TEC measurements are calculated using the rapid precise GPS orbits provided by

156    the Crustal Dynamics Data Information System (CDDIS)

157    (https://cddis.nasa.gov/archive/gnss/products/), and the resulting geolocated vTEC perturbations

158    are mapped for the entire day of January 15, 2022. The resulting vTEC measurements are then

159    plotted on maps according to their IPP location for every minute of the day. Example maps and

160    videos of vTEC anomalies are provided in the supplementary material.

161       To compare the propagation of the ionospheric waves to those at the surface, a barotropic

162    version of the TIGAR (Transient Inertia Gravity and Rossby wave dynamics) model has been

163    run at T170 horizontal resolution. TIGAR solves primitive equations on the sphere using the

164    Hough harmonics [Vasylkevych and Žagar, 2021] thereby providing the time evolution of

165    Rossby and inertia-gravity waves. The atmospheric response to the Tonga eruption is simulated

166    using a homogeneous background (i.e. isothermal and with no winds). The eruption is

167    represented by a Gaussian perturbation at the location of the eruption superimposed on the

168    barotropic atmosphere with a mean depth of 10,114 km. The simulated horizontally-propagating

169    gravity waves represent the Lamb wave in the hydrostatic, isothermal atmosphere. The mean

170     depth and the parameters of the source were chosen to fit the observed horizontal structure of the

171     eruption and the observed amplitude and timing of surface pressure perturbations.

172        One method to look at the global propagation of ionospheric disturbances induced by a

173     known source is to organize the vTEC anomalies according to their distance from the source, as

174     in Chen et al. [2017] to characterize earthquake-driven ionospheric TIDs. By binning all vTEC

175     anomalies with latitudes between $55^o$S and $55^o$N in 50km bins with respect to radial distance

176     from the eruption location, we can isolate coherent structures associated with the event. We have

177     focused here on regions below $55^o$ since the high degree of other activity at the poles

178     significantly complicates the identification of waves. This approach is applied in Figure 2A,

179     where we see several strong vTEC anomaly structures fanning out from the eruption epicenter

180     (y-axis) and from the time of eruption onset (x-axis). Note that the color scale has been saturated

181     at 0.2 TECU to make wave features easier for the reader to see. Wave amplitudes should instead

182     be inferred from individual station measurements to avoid attenuation/smearing from data

183     binning. Also plotted in Figure 2a, is a superposition of the radial propagation of the pressure

184     disturbance originating from the eruption. This pressure wave propagates at 315 ms$^{-1}$ and is

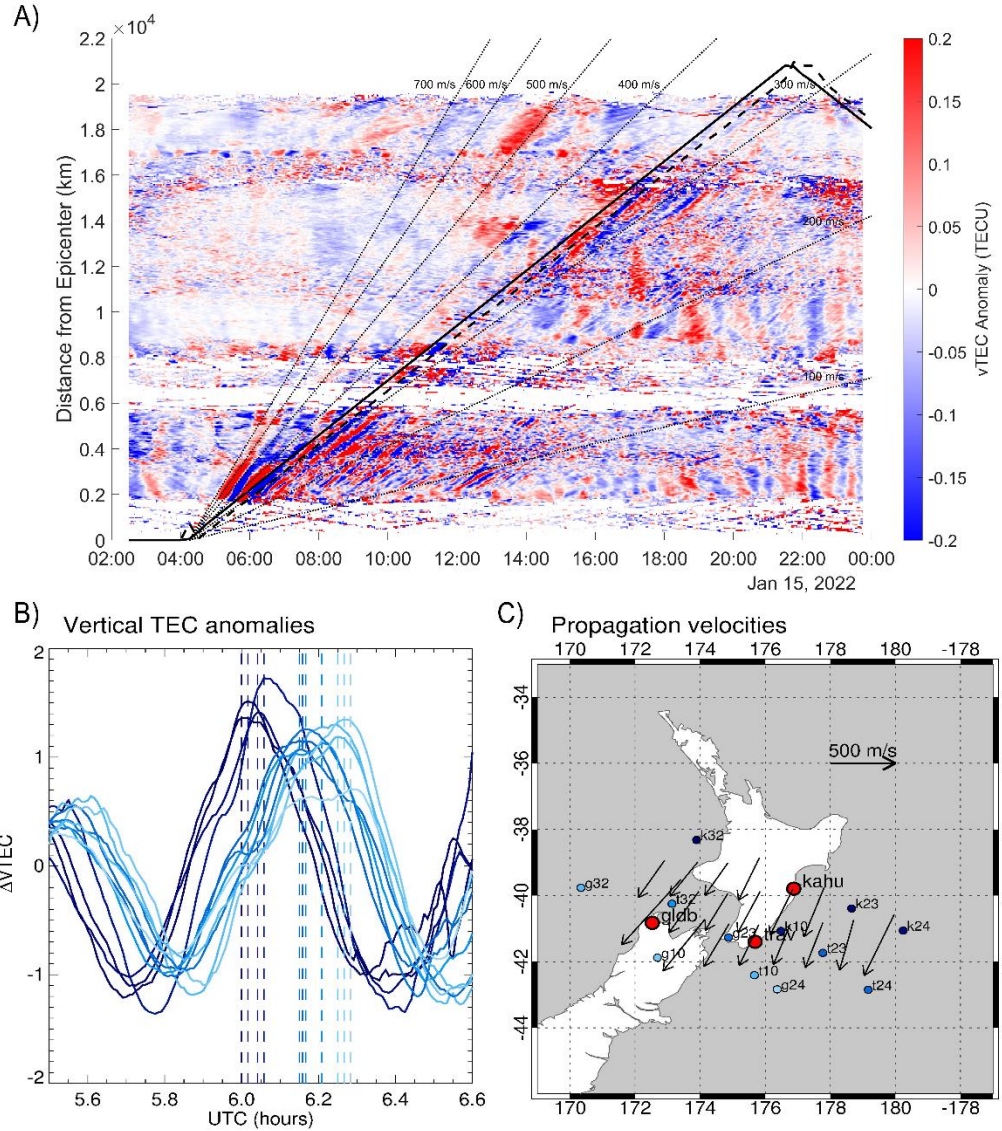185     coherent with the generation and propagation of primary MSTIDs from the event.

186

**Figure 2. A)** *vTEC anomaly averaged in 100km bins of radial distance from the Tonga eruption*
*epicenter. The barotropic model height anomaly peak and depression are plotted in solid and dashed*
*black lines. Dotted black lines correspond to trajectories for fixed radial speeds from 100 ms⁻¹ to 700 ms⁻¹*
*in increments of 100 ms⁻¹.* ***B)*** *Demonstration of perturbation front tracking used to determine the velocity*
*estimates in C for a subset of New Zealand stations.* ***C)*** *Demonstration of the velocity estimates (arrows)*
*determined using the triangulation method for a subset of three New Zealand stations. Colored blue dots*
*are IPP locations at time of VTEC anomaly maximum.*

To assess the speed of the disturbances propagating from the eruption event, we use two

main methods. The first method is to use triangulation of the irregularities from neighboring

11

198     GNSS raypaths. If the TEC signature of a travelling ionospheric disturbance is detected along at

199     least three GPS satellite-receiver raypaths in a localized region, the relative detection time and

200     corresponding IPP locations can be used to estimate the propagation velocity. This method

201     assumes the disturbance has a uniform structure perpendicular to the direction of propagation

202     and requires the assumption of an IPP altitude (400 km), if the altitude of the disturbance is

203     unknown. This TEC triangulation technique has been previously applied in estimating the

204     velocities of ionospheric structures associated with magnetospheric substorms [Watson et al.,

205     2011] and ultra-low frequency magnetic field pulsations [Watson et al., 2015].

206             The second method for characterizing the wave propagation speed is to trace the slope of

207     coherent wave structures in plots of the distance from the epicenter vs time, such as is presented

208     in Figure 2A. One can then use the fitted slope for each independent structure as an estimate of

209     the propagation speed. Separate point populations are used if a coherent wave structure exhibits a

210     break in its slope, such as was seen in Figure 3A at 2200-2300 km before 06:00UT. A

211     demonstration of the result of both speed estimation methods is presented in Figure 3B-C for the

212     regional domain around New Zealand. Using the derived speeds we can also determine an

213     approximate wave generation time by extrapolating the fitted linear trends to zero range. This

214     implied initiation time is used as the x-axis in Figure 3C, not to be confused with the times in

215     Figure 3A-B. Similarly, the triangulated speeds for each wave front can also be averaged and

216     mapped backward to estimate their implied time of origin. Both approaches are done separately

217     for ranges within and beyond 2300 km to highlight the change in phase speed of the waves with

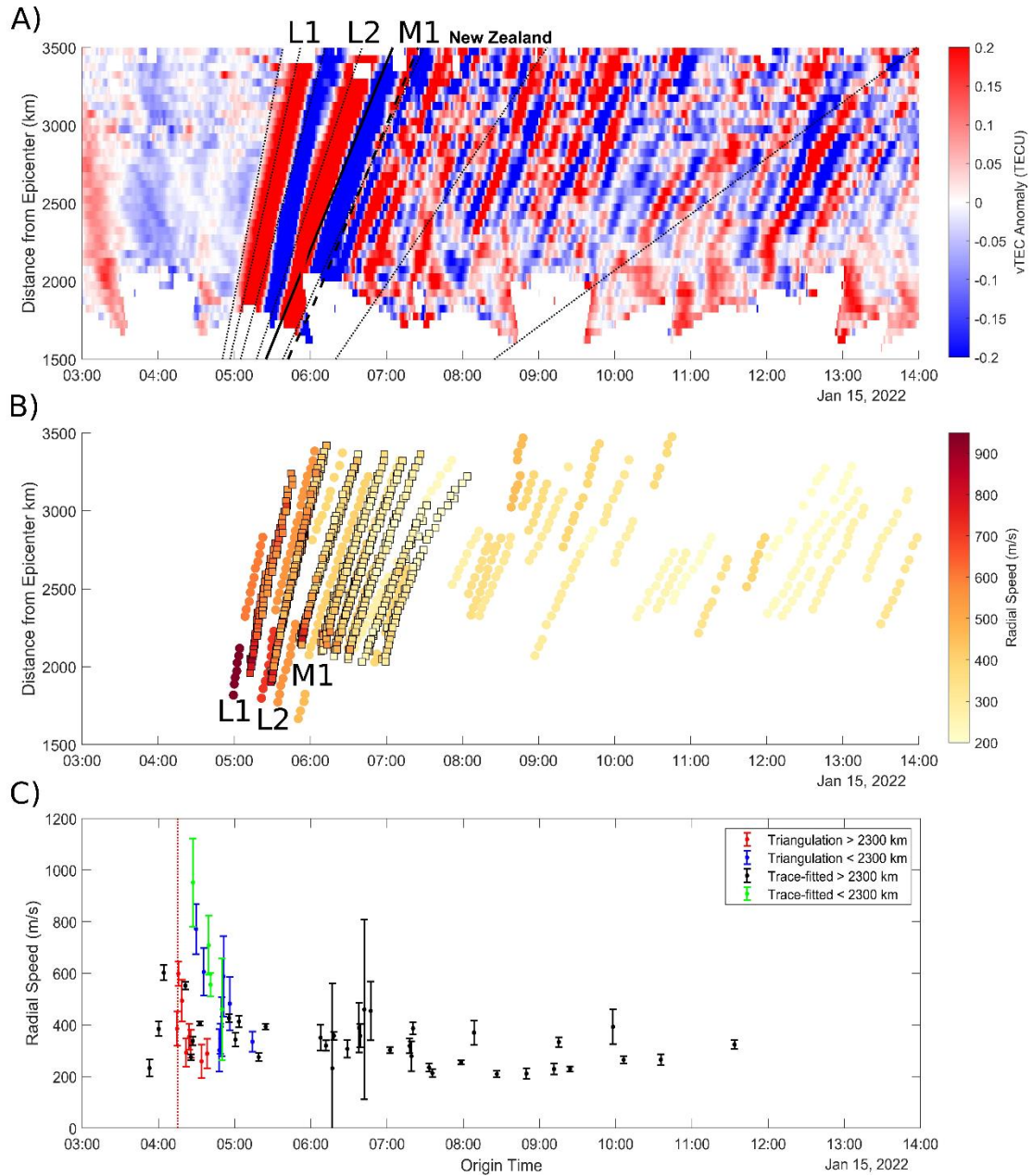218     radial distance from the epicenter.

219

**Figure 3. A)** *Same as Figure 2A, but only using data from within the New Zealand regional domain, marked in Figure 1G.* **B)** *Traces of the leading and trailing null points of TID signatures from panel A colored by the fitted wave speed (circles), and radial distance and time of speed estimates of the triangulation method (squares).* **C)** *Average wave front speeds corresponding to the New Zealand regional domain plotted against estimated time of origin. The beginning of the eruption is marked with a vertical red dashed line. Speeds are color coded according to estimation method and radial distance.*

## Results and Discussion

229

230

231        In Figure 1A-F, we see a number of wave packets arriving at sample GNSS receivers at

232    roughly the time of the surface pressure anomaly, with the largest amplitudes generally

233    coincident with the surface pressure wave; however, these plots are restrictive and can be

234    challenging to associate directly with the wave fronts propagating from the Tonga eruption.

235        Looking at Figures 2A and 3A-B, we can begin to characterize some of the wave

236    structures emanating from the Tonga eruption. We first see an LSTID propagating radially at

237    speeds of $950 \pm 170$ ms$^{-1}$, with a wavelength > 1600 km, before slowing substantially to $600 \pm$

238    30 ms$^{-1}$after reaching ~2300 km range (Figure 3B). The trailing edge of this LSTID had a speed

239    of $710 \pm 115$ ms$^{-1}$ before the break at ~2300 km range, where it slows to $550 \pm 15$ ms$^{-1}$. A second

240    LSTID with wavelength of $1350 \pm 100$ km, then propagates from the eruption at $555 \pm 45$ ms$^{-1}$

241    before similarly slowing substantially to $390 \pm 15$ ms$^{-1}$ after ~2500km range. Changes in

242    propagation speed with radial distance can be clearly seen in Figure 3A, where the slopes of

243    LSTID leading/trailing edges abruptly decrease. These breaks in propagation speed can be

244    inferred more directly in Figure 3C by looking at the implied origin times of the waves. LSTIDs

245    within 2300 km of the eruption have origin times of ~15 and ~20 minutes after the eruption,

246    respectively, while the portions of the LSTIDs beyond 2300 km have implied origin times either

247    coincident with the eruption or prior to it, depending on the velocity estimation method. A 15-

248    minute delay is consistent with the time it would take an acoustic wave to propagate into the

249    thermosphere, while there is no indication that LSTIDs were generated at the origin prior to the

250    eruption. The speed of the later portions of the propagation of these TIDs are consistent with

251    horizontally propagating thermospheric gravity waves (e.g. the direct wave) [Mayr et al., 2013].

14

252     Following these two LSTIDs, smaller MSTIDs are seen propagating from the eruption

253     source region for up to six hours. The first of these MSTIDs propagates at a speed of $337 \pm 17$

254     ms$^{-1}$ with an initiation time of 4:32 UT and corresponds almost perfectly with the propagation of

255     a surface pressure wave associated with the eruption (Figure 2A). This first MSTID and the

256     MSTID after it are clearly visible out to ranges of at least 16,000km and have wavelengths of

257     300 to 350 km.  Secondary MSTIDs with wavelengths ranging from 250 to 500 km are also seen

258     generated up to six hours after the passing of the initial pressure disturbance. These secondary

259     MSTIDs have speeds that range from 200 to 400 ms$^{-1}$, with most of the later MSTIDs having

260     speeds toward the lower end of that range, consistent with the characteristics of ducted AGW

261     waves reflected between the Earth and the lower thermosphere [Mayr et al., 2013].

262     The behavior of the ionospheric response to this event appears very similar to that of the

263     2011 Tohoku earthquake, but without the initial Rayleigh Wave [Tsugawa et al., 2011]. Both

264     events see initial LSTIDs with speeds near the ionospheric acoustic speed and subsequent

265     MSTIDs with speeds near the surface acoustic speed.

266     One challenge with looking at the resulting disturbances in the manner shown in Figure

267     2A is that it assumes radial symmetry in the propagation of the TIDs. Many authors have noted

268     preferential directional propagation of these structures associated with earthquakes [Inchin et al.,

269     2020; Zettergren and Snively, 2019, for example]. It is likely that highly directional wave fronts

270     may not be apparent in representations like Figure 2A, which assume isotropy. To get a clearer

271     picture of the wave propagation without batching together all observed stations, in Figure 4 we

272     generate analogous plots to Figure 3A but only for local regions with high GNSS station density.

273     The boundaries of these regions are shown in Figure 1G. Using these plots, we can further

274     examine the extent to which these waves propagate from the source.

275
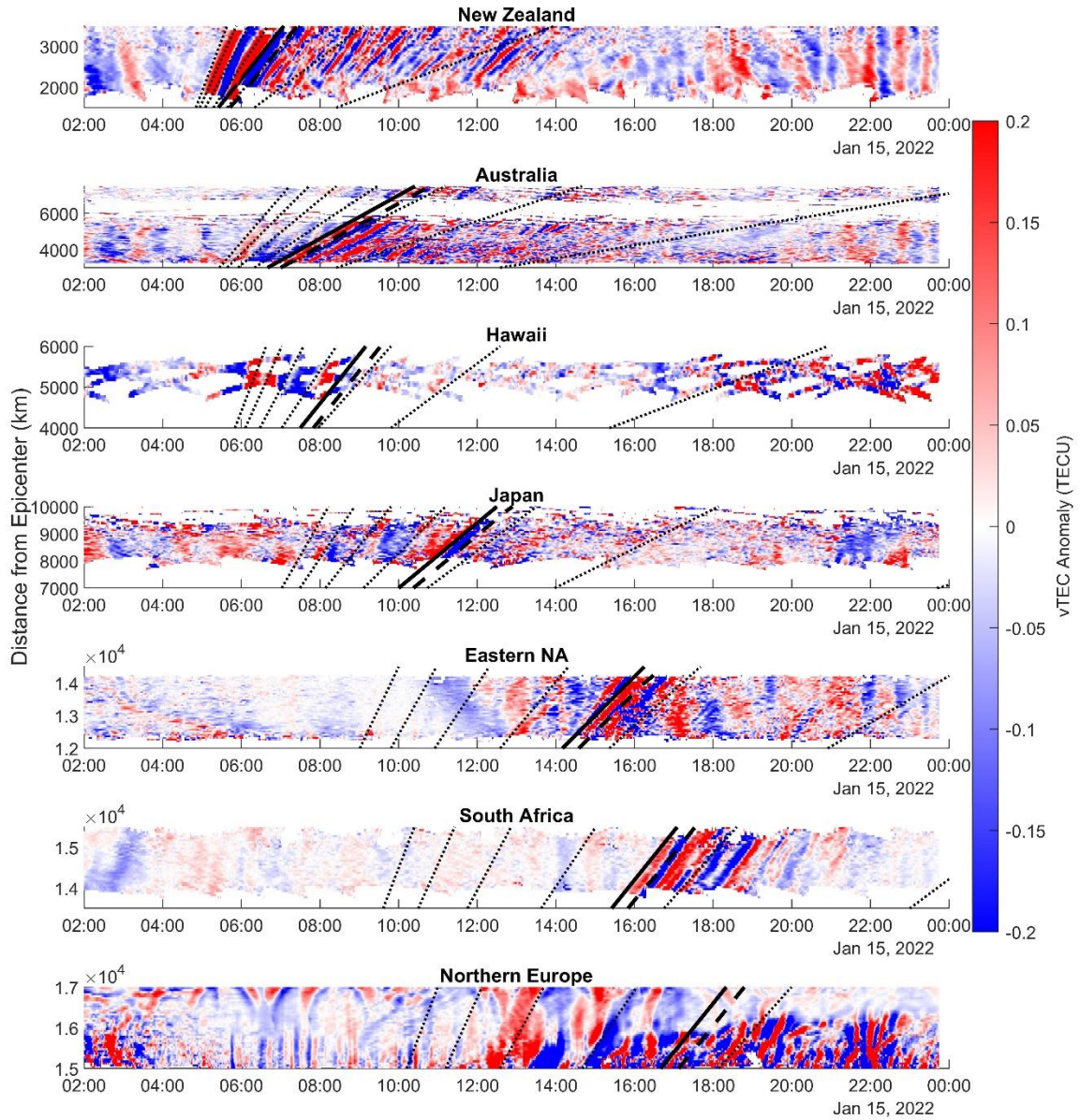


**Figure 4**. *vTEC anomalies plotted against distance from the epicenter for several sub-domain regions, demonstrated in Figure 1G.*

276

277
278

279

280    In Figure 4, we see the abundance of waves of various sizes in the region directly

281    adjacent to the eruption (New Zealand), and we can more clearly track the propagation of

16

282    individual wave fronts. Interestingly, the LSTIDs do not appear to remain coherent in many other

283    regions. Using the dotted propagation speed lines as reference, the first LSTID is seen clearly at

284    New Zealand, Hawaii, and Northern Europe, with more inconclusive observation in Japan and

285    Australia. Contrarily, the first LSTID is not apparent in South Africa and Eastern North America.

286    Much of the same is seen for the second LSTID, but with a much clearer signature in Japan and a

287    candidate signature in Eastern North America. Based on the geomagnetic location of the eruption

288    and previous examinations of TIDs from similar sources, it is expected that waves will

289    preferentially propagate along the magnetic field [Inchin et al., 2020; Zettergren and Snively,

290    2019]. With the eruption being in the southern magnetic hemisphere, this would imply

291    preferential northward propagation of these waves. Similarly, the declination of the magnetic

292    field would imply preferential propagation to the North East and South West, aligned with the

293    magnetic field. Examining Figure 4 again, one may note that the fast LSTID structures are barely

294    discernable in Australia, suggesting substantial attenuation of the waves to the West. These

295    modes are completely absent in South Africa, which is roughly along the same propagation

296    trajectory from the source as Australia. This suggests a substantial disinclination of LSTID

297    propagation to the West from the eruption. In contrast, the first and second LSTID signatures are

298    the dominant structures seen at Hawaii to the North East, near the geomagnetic conjugate point

299    of the eruption site. Interestingly, while the first LSTID front at New Zealand appeared to rapidly

300    slow after ~2300 km range from the source, we see strong LSTID signatures at Hawaii ahead of

301    the 700 ms$^{-1}$ marker and very close to where we would expect a 900 ms$^{-1}$ wave, consistent with

302    the initial LSTID phase speed seen in New Zealand. It appears from this that, while the LSTID

303    slowed substantially as it propagated over New Zealand no such reduction in speed occurred to

304    the North East at Hawaii.

17

305    The appearance of the first and second LSTIDs in Northern Europe, which is at similar

306    magnetic declination to Tonga, is suggestive of highly preferential propagation directly due

307    North of the eruption site; however, a lack of stations in that direction over the Pacific, outside of

308    the auroral oval, makes any conclusions regarding the appearance of the LSTIDs in Northern

309    Europe challenging to assert. The strong presence of the LSTIDs at Hawaii is suggestive;

310    however, more data is necessary. Further conclusions regarding the appearance of these LSTIDs

311    in Northern Europe will thus have to await measurements from alternative sources, such as radio

312    occultation.

313    Subsequent MSTIDs originating from the eruption are seen at five of the seven test

314    locations and arrive at times similar to the modeled atmospheric pressure disturbance. These

315    waves are entirely consistent with AGWs generated from the propagating surface perturbation.

316    The MSTIDs propagating from this disturbance form the dominant global ionospheric wave

317    response from this event, with clear signatures at nearly all sampled GNSS locations. In Northern

318    Europe, MSTID wave signatures of eruption origin are far less obvious, likely due to interaction

319    with waves of auroral origin and the sheer distance from the eruption location; furthermore, at

320    Hawaii the MSTIDs are barely discernable. The lack of clear MSTID signatures at Hawaii may

321    be a product of the lack of stations in that area; however, the observed amplitudes after the

322    passage of the surface pressure anomaly are considerably weaker than the LSTID structures

323    ahead of the surface pressure anomaly, which is only matched at New Zealand. Given that

324    Hawaii is very near to the eruption geomagnetic conjugate point, it is possible that conjugate TID

325    structures, generated by electric field perturbations associated with the TIDs at the eruption

326    location, are interfering with TIDs propagating directly from the eruption [Zettergren and

18

327    Snively, 2019]. This, however, cannot explain why the LSTIDs do not suffer similar interference

328    problems.

329

## Conclusions

330

331         Perhaps the most striking feature of this event is the generation of an initial LSTID with a

332    phase speed of $> 900$ ms$^{-1}$. This wave is generated almost immediately after the event at nearly

333    triple the surface acoustic speed and is close to the acoustic speed at the F-Region peak. This

334    LSTID is shown to rapidly slow to propagation speeds near $700$ ms$^{-1}$ after propagating ~2300 km

335    from the eruption location in the direction of New Zealand but did not exhibit such a reduction in

336    speed at Hawaii, at even further ranges. Whilst the wave is a dominant structure in the vicinity of

337    the eruption location, it appears to quickly dissipate depending on the direction of travel, where it

338    is only barely discernable at Australia 4,000 – 6,000 km to the West of the eruption but forms the

339    dominant wave response at Hawaii at similar ranges to the North East. Interestingly, the structure

340    also seems to appear in Northern Europe between 12:00 UT and 13:00 UT, nearly directly due

341    North from the eruption location. The initial LSTIDs generated from this event are likely

342    acoustic waves generated from the initial eruption shock, while subsequent MSTIDs,

343    propagating near the surface acoustic speed, correspond to AGWs generated by the subsequent

344    atmospheric disturbance and persist to be generated up to six hours after the eruption. While the

345    shock-related LSTIDs demonstrate strong directionality and attenuate much faster than the

346    MSTIDs, the MSTIDs exhibit no clear directional preference and form the dominant wave

347    response seen globally except near the eruption conjugate point where these MSTIDs are much

348    less dominant. Future work will need to combine modeling with additional measurements from

349 radio occultation and of stratospheric/mesospheric winds to further elucidate the mechanisms at

350 play.

351

## Acknowledgements

366

## Availability Statement

368 GNSS data for this study were provided by the following organizations: International GNSS

369 Service (IGS), UNAVCO (https://www.unavco.org/data/gps-gnss/gps-gnss.html), Dutch

20

370    Permanent GNSS Array (http://gnss1.tudelft.nl/dpga/rinex), Can-Net (https://www.can-net.ca/),

371    Scripps Orbit and Permanent Array Center (Garner, http://garner.ucsd.edu/pub/), French Institut

372    Geographique National, Geodetic Data Archiving Facility (GeoDAF,

373    http://geodaf.mt.asi.it/index.html), Crustal Dynamics Data Information System (CDDIS,

374    https://cddis.nasa.gov/archive/gnss/data/daily/), National Geodetic Survey

375    (https://geodesy.noaa.gov/corsdata/), Instituto Brasileiro de Geografia e Estatistica

376    (http://geoftp.ibge.gov.br/informacoes_sobre_posicionamento_geodesico/rbmc/dados/), Instituto

377    Tecnologico Agrario de Castilla y Leon (ITACyL, ftp://ftp.itacyl.es/RINEX/), TrigNet South

378    Africa (ftp://ftp.trignet.co.za), The Western Canada Deformation Array (WCDA,

379    ftp://wcda.pgc.nrcan.gc.ca/pub/gpsdata/rinex), Canadian High Arctic Ionospheric Network

380    (CHAIN, http://chain.physics.unb.ca/chain/pages/data_download), Pacific Northwest Geodetic

381    Array (PANGA, http://www.geodesy.cwu.edu/pub/data/), Centro di Ricerche Sismologiche,

382    Système d'Observation du Niveau des Eaux Littorales (SONEL, ftp://ftp.sonel.org/gps/data),

383    INGV - Rete Integrata Nazionale GPS (RING, http://ring.gm.ingv.it/),RENAG : REseau

384    NAtional GPS permanent (http://rgp.ign.fr/DONNEES/diffusion/), Australian Space Weather

385    Services (https://downloads.sws.bom.gov.au/wdc/gnss/data/),GeoNet New Zealand

386    (https://www.geonet.org.nz/data/types/geodetic), National Land Survey Finland (NLS,

387    https://www.maanmittauslaitos.fi/en/maps-and-spatial-data/positioning-services/rinex-palvelu),

388    SWEPOS Sweden (https://swepos.lantmateriet.se/), Norwegian Mapping Authority (Kartverket,

389    https://ftp.statkart.no/), Geoscience Australia (http://www.ga.gov.au/scientific-

390    topics/positioning-navigation/geodesy/gnss-networks/data-and-site-logs), Institute of

391    Geodynamics, National Observatory of Athens

392    (https://www.gein.noa.gr/services/GPSData/),and European Permanent GNSS Network (EUREF,

393     https://www.epncb.oma.be/_networkdata/data_access/dailyandhourly/datacentres.php).

394     Barotropic TIGAR model simulation output for this study is available at

395     https://doi.org/10.5281/zenodo.5933393.

396

# References

398     Cervera, M. A., and Harris, T. J. (2014), Modeling ionospheric disturbance features in quasi-

399         vertically incident ionograms using 3-D magnetoionic ray tracing and atmospheric gravity

400         waves, J. Geophys. Res. Space Physics, 119, 431– 440, doi:10.1002/2013JA019247.

401     Chen, P., Y. Yao, & W. Yao (2017). On the coseismic ionospheric disturbances after the Nepal

402         Mw7.8 earthquake on April 25, 2015 using GNSS observations. Advances in Space

403         Research, 59(1), 103-113. https://doi.org/10.1016/j.asr.2016.09.021

404     Chou, M.Y., C. H. Lin, J. Yue, L. C. Chang, H.F. Tsai, and C.H. Chen (2017), Medium-scale

405         traveling ionospheric disturbances triggered by Super Typhoon Nepartak (2016), Geophys.

406         Res.Lett.,44, 7569–7577, doi:10.1002/2017GL073961.

407     Coster, A. J., Goncharenko, L., Zhang, S.-R., Erickson, P. J., Rideout, W., & Vierinen, J. (2017).

408         GNSS observations of ionospheric variations during the 21 August 2017 solar eclipse.

409         Geophysical Research Letters, 44, 12,041– 12,048. https://doi.org/10.1002/2017GL075774

410     Dautermann, T., E. Calais, and G. S. Mattioli (2009), Global Positioning System detection and

411         energy estimation of theionospheric wave caused by the 13 July 2003 explosion of the

412         Soufriere Hills Volcano, Montserrat, J. Geophys. Res.,114, B02202,

413         doi:10.1029/2008JB005722

414 Heki, K. (2006), Explosion energy of the 2004 eruption of the Asama Volcano, central Japan,

415     inferred from ionospheric disturbances, Geophys. Res. Lett., 33, L14303,

416     doi:10.1029/2006GL026249.

417 Inchin, P. A., Snively, J. B., Zettergren, M. D., Komjathy, A., Verkhoglyadova, O. P., & Tulasi

418     Ram, S. (2020). Modeling of ionospheric responses to atmospheric acoustic and gravity

419     waves driven by the 2015 Nepal Gorkha earthquake. Journal of Geophysical Research: Space

420     Physics, 125, e2019JA027200. https://doi.org/10.1029/2019JA027200

421 Komjathy, A., Galvan, D.A., Stephens, P., et al. Detecting ionospheric TEC perturbations caused

422     by natural hazards using a global network of GPS receivers: The Tohoku case study. Earth

423     Planet Sp 64, 24 (2012). https://doi.org/10.5047/eps.2012.08.003

424 Komjathy, A., Yang, Y.-M., Meng, X., Verkhoglyadova, O., Mannucci, A. J., and Langley, R. B.

425     (2016), Review and perspectives: Understanding natural-hazards-generated ionospheric

426     perturbations using GPS measurements and coupled modeling, Radio Sci., 51, 951– 961,

427     doi:10.1002/2015RS005910.

428 Ma G, & Maruyama T (2003) Derivation of TEC and estimation of instrumental biases from

429     GEONET in Japan. Ann Geophys 21:2083–2093

430 Mayr, H.G., Harris, I., Varosi, F., Herrero, F.A., 1984a. Global excitation of wave phenomena in

431     a dissipative multiconstituent medium 1. Transfer function of the Earth's thermosphere. J.

432     Geophys. Res. 89, 10929–10959.

433 Mayr, H.G., Harris, I., Varosi, F., Herrero, F.A., 1984b. Global excitation of wave phenomena in

434     a dissipative multiconstituent medium 2. Impulsive perturbations in the Earth's thermosphere.

435     J. Geophys. Res. 89, 10961–10986.

436     Mayr, H.G., E.R. Talaat, & B.C. Wolven (2013). Global propagation of gravity waves generated

437          with the whole atmosphere transfer function model, Journal of Atmospheric and Solar-

438          Terrestrial Physics, 104, 7-17, https://doi.org/10.1016/j.jastp.2013.08.001

439     Nishioka, M., Tsugawa, T., Kubota, M., and Ishii, M. (2013), Concentric waves and short-period

440          oscillations observed in the ionosphere after the 2013 Moore EF5 tornado, Geophys. Res.

441          Lett., 40, 5581– 5586, doi:10.1002/2013GL057963

442     Savastano, G., Komjathy, A., Verkhoglyadova, O. et al. Real-Time Detection of Tsunami

443          Ionospheric Disturbances with a Stand-Alone GNSS Receiver: A Preliminary Feasibility

444          Demonstration. Sci Rep 7, 46607 (2017). https://doi.org/10.1038/srep46607

445     Themens, D.R., P.T. Jayachandran, R.B. Langley, J.W. MacDougall, and M.J. Nicolls (2013).

446          Determining Receiver Biases in GPS-derived Total Electron Content in Auroral Oval and

447          Polar Cap Region Using Ionosonde Measurements. GPS Solutions, 17(3), pp. 357-369, doi:

448          10.1007/s10291-012-0284-6

449     Themens, D. R., P.T. Jayachandran, M.J. Nicolls, and J.W. MacDougall (2014), A top to bottom

450          evaluation of IRI 2007 within the polar cap, J. Geophys. Res. Space Physics, 119, 6689–

451          6703, doi:10.1002/2014JA020052.

452     Tsugawa, T., Saito, A., Otsuka, Y. et al. (2011). Ionospheric disturbances detected by GPS total

453          electron content observation after the 2011 off the Pacific coast of Tohoku Earthquake. Earth

454          Planet Sp 63, 66. https://doi.org/10.5047/eps.2011.06.035

455     Vasylkevych, S, Žagar, N. A high-accuracy global prognostic model for the simulation of

456          Rossby and gravity wave dynamics. Q J R Meteorol Soc. 2021; 1989– 2007.

457          https://doi.org/10.1002/qj.4006

458 Watson, C., Jayachandran, P. T., Spanswick, E., Donovan, E. F., and Danskin, D. W. (2011),

459     GPS TEC technique for observation of the evolution of substorm particle precipitation, J.

460     Geophys. Res., 116, A00I90, doi:10.1029/2010JA015732.

461 Watson, C., Jayachandran, P. T., Singer, H. J., Redmon, R. J., and Danskin, D. (2015), Large-

462     amplitude GPS TEC variations associated with Pc5–6 magnetic field variations observed on

463     the ground and at geosynchronous orbit, J. Geophys. Res. Space Physics, 120, 7798– 7821,

464     doi:10.1002/2015JA021517.

465 Zawdie, K. A., Drob, D. P., Huba, J. D., and Coker, C. (2016), Effect of time-dependent 3-D

466     electron density gradients on high angle of incidence HF radiowave propagation, Radio Sci.,

467     51, 1131– 1141, doi:10.1002/2015RS005843.

468 Zettergren, M. D., & Snively, J. B. (2019). Latitude and longitude dependence of ionospheric

469     TEC and magnetic perturbations from infrasonic-acoustic waves generated by strong seismic

470     events. Geophysical Research Letters, 46, 1132– 1140.

471     https://doi.org/10.1029/2018GL081569

472 Zhang, S.-R., Erickson, P. J., Coster, A. J., Rideout, W., Vierinen, J., Jonah, O. F., &

473     Goncharenko, L. P. (2019). Subauroral and polar traveling ionospheric disturbances during

474     the 7–9 September 2017 storms. Space Weather, 17, 1748– 1764.

475     https://doi.org/10.1029/2019SW002325

476

477

478